

Virtual Photons Shed Light on the Early Temperature of Dense QCD Matter

Jessica Churchill,¹ Lipei Du,¹ Charles Gale,¹ Greg Jackson,^{2,3} and Sangyong Jeon¹

¹*Department of Physics, McGill University, 3600 University Street, Montreal, QC H3A 2T8, Canada*

²*Institute for Nuclear Theory, Box 351550, University of Washington, Seattle, WA 98195-1550, United States*

³*SUBATECH, Nantes Université, IMT Atlantique, IN2P3/CNRS,*

4 rue Alfred Kastler, La Chantrerie BP 20722, 44307 Nantes, France

(Dated: February 20, 2024)

Dileptons produced during heavy-ion collisions represent a unique probe of the QCD phase diagram, and convey information about the state of the strongly interacting system at the moment their preceding off-shell photon is created. In this study, we compute thermal dilepton yields from Au+Au collisions performed at different beam energies, employing a (3+1)-dimensional dynamic framework combined with emission rates accurate at next-to-leading order in perturbation theory and which include baryon chemical potential dependencies. By comparing the effective temperature extracted from the thermal dilepton invariant mass spectrum with the average temperature of the fluid, we offer a robust quantitative validation of dileptons as effective probe of the early quark-gluon plasma stage.

Introduction. — To clarify the many-body properties of quantum chromodynamics (QCD), like its emergent phases and their boundaries, remains a chief objective in nuclear physics [1]. Relativistic nuclear collisions as performed and studied in terrestrial laboratories constitute the only means to explore the properties of QCD matter under extreme but controlled conditions [2]. The data generated by these events can then be used to inform our understanding of QCD, and to push further the extent of our knowledge. These explorations come with significant challenges. For one, systems generated in heavy-ion collisions are highly dynamic and short-lived, evolving over mere yoctoseconds [3]. The trajectory of the strongly interacting system across the QCD phase diagram, from birth of the quark-gluon plasma (QGP) to emergence of confined hadrons, is complex and comprises various stages. To decipher the properties of the transient nuclear matter, an advanced multistage framework is required, and the resulting predictions must be compared to sophisticated many-body experimental observables [4–11].

The fact that hadrons interact strongly with the medium makes them mostly sensitive to the late stages of the evolution; this complicates the extraction of information about the early stage of QGP evolution from hadronic measurements. Electromagnetic probes are not handicapped in the same way: Real and virtual photons get generated continuously throughout the entire collision evolution, but unlike hadrons, they remain unaltered by the strong interactions once emitted [12–16]. This distinctive feature has made them exceptional tools for investigating the early-stage QGP [17–19]. Among electromagnetic probes, lepton pairs (dileptons) resulting from the decay of virtual photons, are especially useful as their invariant mass renders their spectrum impervious to flow effects, unlike that of real photons which can be altered by Doppler shifts [20, 21] [22]. Thus, dileptons are usually considered a reliable thermometer for assessing the

properties of the hot and dense QCD medium [23, 24], even if their emission rate is suppressed over that of real photons by a factor of the fine structure constant, α_{em} . Nonetheless, it’s important to acknowledge that dileptons are generated at various stages of the collision fireball [18, 19], wherein the temperature undergoes significant fluctuations both in space and time. Therefore, there remains a need to establish a clear connection between the effective temperatures derived from dileptons and the underlying physical properties of the medium. That connection, which requires delicate modeling, is the purpose of this paper.

Specifically, our goal is to investigate the fidelity of dilepton spectra as “thermometers” of the excited partonic medium formed in nucleus-nucleus collisions at energies of the Relativistic Heavy-Ion Collider (RHIC), from the Beam Energy Scan (BES) regime to the top RHIC energy: $\sqrt{s_{\text{NN}}} = 7.7 - 200$ GeV. In order to compute the dilepton yields originating from the baryon-charged QCD medium existing at collision energies on the low side of this range, we utilise the dilepton emission rate at next-to-leading order (NLO) with nonzero baryon chemical potential. We compare values of the temperature extracted from dilepton spectra in the intermediate invariant mass region (IMR), $1 \text{ GeV} \leq M \leq 3 \text{ GeV}$ [25], with the “true” values occurring in the (3+1)-dimensional dissipative hydrodynamics that is tuned to reproduce the hadronic measurements. In so doing, we establish a reliable connection between the effective temperatures extracted from dileptons and the fundamental physical properties of the QCD medium.

Thermal dilepton radiation. — The yield of emitted thermal dileptons, can be obtained from the time and volume integrated rate of a QGP that has attained *local* thermal equilibrium. We let $T(X)$, $\mu_B(X)$ and $u^\mu(X)$ describe the local temperature, baryon chemical potential and flow velocity of the plasma respectively, where $X = (t, \mathbf{x})$ is a spacetime coordinate. Conservation of

energy, momentum, and baryon current dictate the hydrodynamic evolution of the system [26–28], with viscous corrections controlled by transport coefficients [27, 29], and as constrained by an equation of state [30].

In finite-temperature field theory, the fully differential rate is related to the in-medium self-energy of the photon, $\Pi^{\mu\nu}$ [31, 32], which is calculated as a function of the dilepton’s energy, ω , and momentum, \mathbf{k} , in the local rest frame. As such, they are spacetime dependent:

$$\omega(X) = K_\mu u^\mu(X), \quad k(X) = \sqrt{\omega(X)^2 - M^2},$$

where $K^\mu = (M_\perp \cosh y, \mathbf{k}_\perp, M_\perp \sinh y)$ is the (measured) four-momentum of the dilepton, in the lab frame, with the z -direction aligned parallel to the axis of the colliding nuclei, $M_\perp \equiv \sqrt{M^2 + k_\perp^2}$ is the transverse mass and, y being the rapidity. The yield with respect to M and y can be expressed as

$$\frac{dN}{dM dy} = \frac{\alpha_{\text{em}}^2}{3\pi^3 M} \left\{ \sum_{i=1}^{n_f} Q_i^2 \right\} B\left(\frac{m_\ell^2}{M^2}\right) \times \int d^2\mathbf{k}_\perp \int d^4X \frac{\text{Im} \Pi_\mu^\mu(\omega(X), k(X))}{\exp(\omega(X)/T(X)) - 1}, \quad (1)$$

where the quark charge-fractions are Q_i (in units of the electron charge), and the kinematic factor to produce the pair of leptons is $B(x) \equiv (1 + 2x)\sqrt{1 - 4x}$ if $x < \frac{1}{4}$, otherwise $B(x) \equiv 0$. Three light flavours are assumed, i.e. $n_f = 3$, implying that $\sum_i Q_i^2 \rightarrow \frac{2}{3}$. And since we focus on the IMR, the lepton masses can be set to zero ($m_\ell = 0$) and $B \simeq 1$ in Eq. (1).

The rates can be derived from the imaginary part of the retarded photon self-energy [32–34]. We evaluate the QCD corrections to the dilepton emission rate in perturbation theory and include non-zero values of the baryon chemical potential μ_B [35]. For intermediate masses M , it becomes necessary to interpolate between two regimes [36], namely: *i*) for $M \gtrsim T$, and *ii*) for $M \lesssim \sqrt{\alpha_s} T$. In the former case, strict order-by-order perturbation theory can be used, see Π^{LO} and Π^{NLO} in Fig. 1, but this approach breaks down as the mass M becomes ‘parametrically’ small [37]. The upshot is that arbitrary orders in α_s are needed to describe both screening via hard thermal loop (HTL) insertions [38], in addition to the Landau-Pomeranchuk-Migdal (LPM) effect [39–42]. This resummation can be performed rigorously for $M \rightarrow 0$, involving ladder diagrams as shown in Fig. 1, but only includes an approximate form of the strict one and two-loop self energy [when formally re-expanded to $\mathcal{O}(1)$ and $\mathcal{O}(\alpha_s)$ respectively]. Therefore, we marry regime *i*) with regime *ii*) by using the full LO and NLO expressions and only keeping the higher order parts of the LPM result [43]. The higher order LPM corrections are necessary to obtain a finite result when $M = 0$, and near this point they serve to compensate the remnant of an unphysical log divergence in $\text{Im} \Pi^{\text{NLO}}$ for $M \rightarrow 0^\pm$ [44–48]. Far away

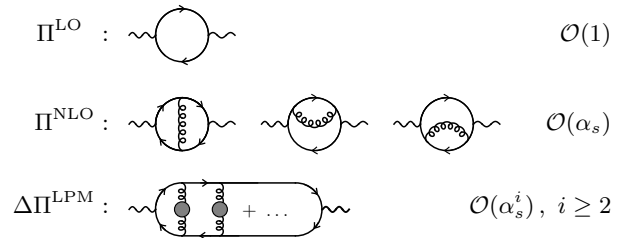


Figure 1. The perturbative diagrams included in our evaluation. For the LPM class of ladder diagrams, HTL indicates that rungs are screened with HTL gluon self-energies while it should be understood that the valence quarks are evaluated at their asymptotic thermal mass.

from the lightcone, the LPM corrections are formally not justified, but remain negligible next to the LO and NLO parts [49–51].

With these considerations in mind, we adopt the full resummed spectral function [52], defined by

$$\text{Im} \Pi_{\text{resummed}}^{\text{NLO}} = \text{Im} [\Pi^{\text{LO}} + \Pi^{\text{NLO}} + \Delta\Pi^{\text{LPM}}]. \quad (2)$$

The formal power counting in α_s is indicated in Fig. 1, although it should be noted that collinear singularities reorganise the naive interpretation of certain diagrams [42]. Each ingredient in (2) needs to be evaluated numerically, for which the details can be found in Ref. [35]. For the QCD coupling, we use the fixed value $\alpha_s = 0.3$ which is motivated in Sec. of the Supplementary Material [53] (where we also comment on the overall accuracy of perturbation theory in the IMR).

The integration in Eq. (1) is performed over a (3+1)-dimensional fluid dynamical evolution [54, 55], with four-volume element $d^4X = \tau d\tau d\eta_s d^2\mathbf{x}_\perp$ where τ is the longitudinal proper time and η_s is the spacetime rapidity, specifically calibrated to reproduce the *hadronic* data measured at the energies discussed in this paper [35, 56]. The hydrodynamical framework includes both shear viscosity and baryon diffusion, but bulk viscosity is neglected and the dilepton emission rates themselves are not corrected for viscous effects [57]. We integrate k_\perp over a range sufficient for comparison with the acceptance-corrected excess spectra measured by the STAR Collaboration [58–61]. Since this study focuses on thermal dileptons originating from the QGP, we specifically consider fluid cells with temperatures exceeding the freeze-out line as established in Ref. [62]. This demarcation closely aligns with the chemical freeze-out line determined by the STAR Collaboration [63], and we attribute the thermal dileptons emitted from the fluid cells below this line to contributions from hadronic matter. In Fig. 2, one can see that the calculated thermal signal is in fact in quantitative agreement with measurements performed by the STAR Collaboration [58–61], once the background contributions [64] have been subtracted. While μ_B in-

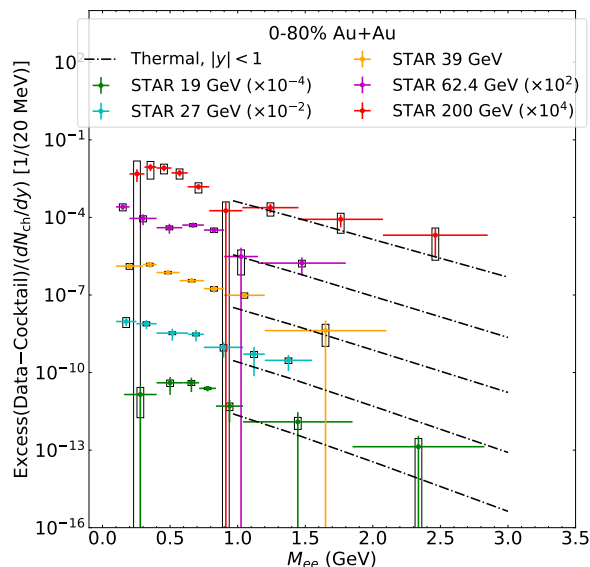


Figure 2. Dielectron excess mass spectra within rapidity $|y| < 1$, normalized by midrapidity charged hadron multiplicity dN_{ch}/dy , for 0–80% Au+Au collisions at $\sqrt{s_{\text{NN}}} = 19, 27, 39, 62.4, 200$ GeV. The markers with error bars and open boxes indicate the STAR experimental measurements with statistical and systematic uncertainties, while the dot-dashed lines represent model calculations.

creases at lower beam energies, the corresponding dependence in the emission rate leaves little imprint of this on the dilepton spectra themselves because a majority of the QGP fluid satisfies $\mu_{\text{B}}/T \lesssim 3$ within $|\eta_s| < 1$ even at a beam energy of 7.7 GeV.

Probing the early QGP temperature.— In our longer companion paper [35], we establish the effectiveness of the temperature extraction method using the thermal dilepton spectra within the IMR as a proxy for the temperatures of the fluid cells. That region of dilepton invariant mass is chosen to highlight the signal coming from the QGP phase, as lower invariant masses are known to receive important contributions from reactions involving composite hadrons [65]. Furthermore, the perturbative scheme in Eq. (2) is well suited for this mass range with an estimated theoretical uncertainty comfortably below $\sim 10\%$.

The approximate large- M behaviour of the rate, $d\Gamma/dM \sim (MT)^{3/2} \exp(-M/T)$, motivates defining an effective temperature T_{eff} by assuming that the integrated spectrum dN/dM follows a similar functional form in the IMR. We perform an analysis where we derive T_{eff} from dilepton spectra at each time step, and then examine how it relates to the evolving hydrodynamic temperatures as functions of proper time. Figure S2 in the Supplementary Material [53] clearly illustrates that T_{eff} closely tracks the mean hydrodynamic temperature $\langle T \rangle$ as a function of proper time, reflecting the cooling of the

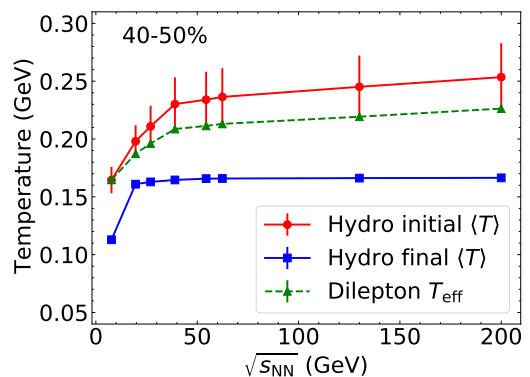


Figure 3. Initial temperatures (red dots) and final temperatures (blue squares) of the hydrodynamic evolution, along with effective temperatures derived from dilepton spectra (green triangles) for 40–50% Au+Au collisions, presented as a function of beam energy. The error bars associated with the hydrodynamic temperatures indicate standard deviations, while the error bars of the effective temperatures represent uncertainties resulting from the fitting procedure in the temperature extraction method.

expanding QGP fireball. The close alignment between T_{eff} and $\langle T \rangle$ provides another compelling validation of the temperature extraction method, although we see that T_{eff} is consistently above $\langle T \rangle$ throughout the evolution.

Building upon these validations, we apply the same temperature extraction method to determine T_{eff} from the spacetime-integrated thermal dilepton spectra seen in Fig. 2. To make the most of T_{eff} as a reliable thermometer for the QGP fireball, we further investigate its connection with the initial temperatures $\langle T_{\text{in}} \rangle$, marking the beginning of the hydrodynamic expansion, and final freeze-out temperatures $\langle T_{\text{f}} \rangle$ across the eight beam energies. This is illustrated in Fig. 3 (for 40–50% centrality), which includes the initial temperature variations originating from both short-range lumpy fluctuations, and long-range gradients on the system scale. (The latter is the dominant factor, which shrinks with lower beam energies because of the lower temperatures at the fireball’s center.) Figure 3 shows that the final freeze-out temperature remains relatively stable down to $\sqrt{s_{\text{NN}}} = 19$ GeV but experiences a sudden drop at 7.7 GeV. This decline is due to the significantly higher μ_{B}/T for this beam energy, which, at the phase transition, accompanies a lower freeze-out temperature. The picture is consistent across other centrality classes (not shown), which are primarily determined by the characteristics of the freeze-out line [62, 63].

While we do not find a significant correlation between T_{eff} and $\langle T_{\text{f}} \rangle$, it appears that T_{eff} is proportional to $\langle T_{\text{in}} \rangle$. Figure 3 indicates that, as the beam energy decreases, both T_{eff} and $\langle T_{\text{in}} \rangle$ display similar behaviour and tend to approach each other; again, these trends are consistently observed across various centralities. This observation, which was anticipated on theoretical grounds [13, 15],

motivates us to investigate the relationship between the initial mean temperature $\langle T_{\text{in}} \rangle$ and the effective temperature T_{eff} in Au+Au collisions at a range of beam energies and centralities. Figure 4 demonstrates a linear relationship between the initial mean temperature and the effective temperature,

$$\langle T_{\text{in}} \rangle = \kappa T_{\text{eff}} + c, \quad (3)$$

where a global fit yields the parameters

$$\kappa = 1.55 \pm 0.02, \quad c = -(9.3 \pm 0.3) \times 10^{-2} \text{ GeV}.$$

This linear relationship presents a reliable—and currently unique—means of extracting the early temperatures of the hot and dense nuclear matter, utilizing the effective temperature derived from dilepton spectra, immune to the distortions caused by Doppler effects. Despite the initial temperature variations depicted in Fig. 3, the definition of mean temperature inherently integrates out these fluctuations, and the obtained $\langle T_{\text{in}} \rangle$ is impervious to significant uncertainties via Eq. (3). Let us emphasize that $\langle T_{\text{in}} \rangle$ should thus be interpreted as the central value of some broad distribution, whose statistical variance is relatively large (see Fig. S2 of the supplementary material [53]). The quoted standard errors, on κ and c , are due to the fitting procedure alone. There exist global studies to address and incorporate systematic model uncertainties [4–7]; future such investigations will incorporate the emission of electromagnetic radiation. Importantly, as far as the emission rates are concerned, we find negligible variations in T_{eff} from fixing the QCD perturbative coupling.

Several insights can be drawn from the results presented in Fig. 4. First and foremost, the unmistakable correlation between T_{eff} and $\langle T_{\text{in}} \rangle$, as opposed to the final mean temperature, naturally finds its explanation in the spacetime evolution of dilepton production within a rapidly expanding QGP fireball. As highlighted in our companion paper [35], dilepton production is suppressed over time because the temperature drops too fast for the expanding volume to compensate. Hence, the IMR of dilepton spectra are predominantly influenced by the early stages of QGP evolution and are notably insensitive to the late-stage expansion.

Furthermore, uncertainties in T_{eff} tend to grow slightly with $\sqrt{s_{\text{NN}}}$ for a specific centrality class or when transitioning from peripheral to central collisions at a given beam energy. This trend can be attributed to several factors, including the extended lifetime of the QGP at higher beam energies or in central collisions, combined with more substantial temperature variations during its evolution (see also Fig. S2 in the Supplementary Material [53]). As a result, the dilepton spectra exhibit more pronounced deviations from the profiles associated with a specific effective temperature.

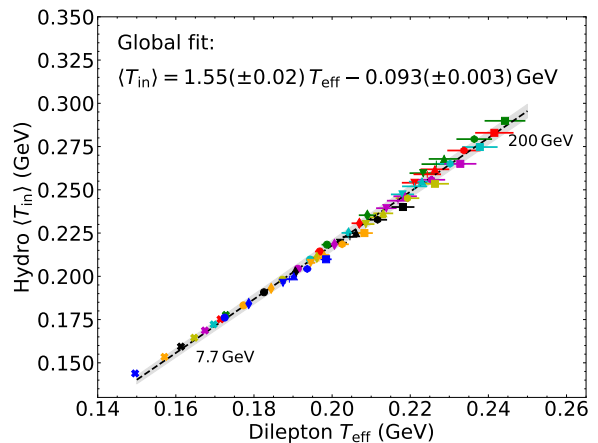


Figure 4. Correlation between initial average hydrodynamic temperatures $\langle T_{\text{in}} \rangle$ and the derived effective temperature T_{eff} from dilepton spectra for Au+Au collisions at eight beam energies, spanning from 7.7 to 200 GeV, within centrality bins from 0–10% to 70–80% (see the Supplemental Material [53] for a table containing all data points). The black dashed line denotes a global fit to all data points, and the gray band illustrates the uncertainties associated with the fitting procedure.

Finally, we emphasize that our study primarily focuses on thermal dileptons due to the QGP, whose evolution is described via dissipative hydrodynamics. At the lower end of the considered beam energies, due to the substantial time required for the two colliding nuclei to fully interpenetrate, the pre-hydrodynamic stage becomes non-negligible and it is reasonable to assume that its contribution to the dilepton yields increases accordingly. In a more suitable dynamical initialization scenario, energy continues to be deposited into the collision fireball, causing the temperature to increase until it reaches a maximum value when the two colliding nuclei have completely traversed each other [66]. Subsequently, this is followed by the onset of a pure hydrodynamic QGP expansion. Thus, the maximum temperature of the pre-hydrodynamic stage and its corresponding time should be treated as the initial temperature and starting time for the hydrodynamic evolution in our study. Examining the influence of the pre-hydrodynamic stage on dilepton spectra and its impact on the associated effective temperature is a topic worthy of dedicated research which we leave for future investigations.

Conclusions.— From the studies reported here, using state-of-the-art lepton pair emissivities and sophisticated (3+1)-dimensional dissipative fluid dynamical modeling, it is clear that the electromagnetic radiation measured in relativistic nuclear collisions fulfills its promise of providing penetrating tomographic information of the strongly interacting medium, particularly in serving as a thermometer for the early-stage QGP. Complementary to the findings in Ref. [67] that established

the general correlation between initial state energy and measured particle multiplicities, as well as in Ref. [68] where the initial baryon density was constrained using rapidity-dependent directed flows, our research provides a solid means of probing the phase diagram of hot and dense nuclear matter, via the slope of dilepton spectra in the IMR and at several beam energies and centrality classes. As such, our research contributes to filling in an essential piece of the puzzle, enhancing our understanding of QCD matter and its manifestation in heavy-ion experiments.

Acknowledgements.— We acknowledge very useful conversations with Bailey Forster, Han Gao, and Jean-François Paquet. This work was funded in part by the U. S. Department of Energy (DOE), under grant No. DE-FG02-00ER41132 (G. J.), in part by the Agence Nationale de la Recherche, under grant ANR-22-CE31-0018 (AUTOTHERM) (G. J.), and in part by the Natural Sciences and Engineering Research Council of Canada (J. C., L. D., C. G., S. J.). Computations were made on the Béluga supercomputer system from McGill University, managed by Calcul Québec and the Digital Research Alliance of Canada.

-
- [1] P. Braun-Munzinger and J. Wambach, “The Phase Diagram of Strongly-Interacting Matter,” *Rev. Mod. Phys.* **81**, 1031–1050 (2009), [arXiv:0801.4256 \[hep-ph\]](#).
- [2] Adam Bzdak, Shinichi Esumi, Volker Koch, Jinfeng Liao, Mikhail Stephanov, and Nu Xu, “Mapping the Phases of Quantum Chromodynamics with Beam Energy Scan,” *Phys. Rept.* **853**, 1–87 (2020), [arXiv:1906.00936 \[nucl-th\]](#).
- [3] Edward Shuryak, “Strongly coupled quark-gluon plasma in heavy ion collisions,” *Rev. Mod. Phys.* **89**, 035001 (2017), [arXiv:1412.8393 \[hep-ph\]](#).
- [4] Jonah E. Bernhard, J. Scott Moreland, and Steffen A. Bass, “Bayesian estimation of the specific shear and bulk viscosity of quark-gluon plasma,” *Nature Phys.* **15**, 1113–1117 (2019).
- [5] D. Everett *et al.* (JETSCAPE), “Phenomenological constraints on the transport properties of QCD matter with data-driven model averaging,” *Phys. Rev. Lett.* **126**, 242301 (2021), [arXiv:2010.03928 \[hep-ph\]](#).
- [6] Govert Nijs, Wilke van der Schee, Umut Gürsoy, and Raimond Snellings, “Transverse Momentum Differential Global Analysis of Heavy-Ion Collisions,” *Phys. Rev. Lett.* **126**, 202301 (2021), [arXiv:2010.15130 \[nucl-th\]](#).
- [7] Matthew R. Heffernan, Charles Gale, Sangyong Jeon, and Jean-François Paquet, “Bayesian quantification of strongly-interacting matter with color glass condensate initial conditions,” (2023), [arXiv:2302.09478 \[nucl-th\]](#).
- [8] H. Niemi, K. J. Eskola, and R. Paatelainen, “Event-by-event fluctuations in a perturbative QCD + saturation + hydrodynamics model: Determining QCD matter shear viscosity in ultrarelativistic heavy-ion collisions,” *Phys. Rev. C* **93**, 024907 (2016), [arXiv:1505.02677 \[hep-ph\]](#).
- [9] H. Hirvonen, K. J. Eskola, and H. Niemi, “Flow correlations from a hydrodynamics model with dynamical freeze-out and initial conditions based on perturbative QCD and saturation,” *Phys. Rev. C* **106**, 044913 (2022), [arXiv:2206.15207 \[hep-ph\]](#).
- [10] J. E. Parkkila, A. Onnerstad, S. F. Taghavi, C. Mordasini, A. Bilandzic, M. Virta, and D. J. Kim, “New constraints for QCD matter from improved Bayesian parameter estimation in heavy-ion collisions at LHC,” *Phys. Lett. B* **835**, 137485 (2022), [arXiv:2111.08145 \[hep-ph\]](#).
- [11] J. E. Parkkila, A. Onnerstad, and D. J. Kim, “Bayesian estimation of the specific shear and bulk viscosity of the quark-gluon plasma with additional flow harmonic observables,” *Phys. Rev. C* **104**, 054904 (2021), [arXiv:2106.05019 \[hep-ph\]](#).
- [12] Edward V. Shuryak, “Quark-Gluon Plasma and Hadronic Production of Leptons, Photons and Psions,” *Phys. Lett. B* **78**, 150 (1978).
- [13] K. Kajantie and H. I. Miettinen, “Temperature Measurement of Quark-Gluon Plasma Formed in High-Energy Nucleus-Nucleus Collisions,” *Z. Phys. C* **9**, 341 (1981).
- [14] Larry D. McLerran and T. Toimela, “Photon and Dilepton Emission from the Quark - Gluon Plasma: Some General Considerations,” *Phys. Rev. D* **31**, 545 (1985).
- [15] R. C. Hwa and K. Kajantie, “Diagnosing Quark Matter by Measuring the Total Entropy and the Photon Or Dilepton Emission Rates,” *Phys. Rev. D* **32**, 1109 (1985).
- [16] K. Kajantie, Joseph I. Kapusta, Larry D. McLerran, and A. Mekjian, “Dilepton Emission and the QCD Phase Transition in Ultrarelativistic Nuclear Collisions,” *Phys. Rev. D* **34**, 2746 (1986).
- [17] Thomas Peitzmann and Markus H. Thoma, “Direct photons from relativistic heavy ion collisions,” *Phys. Rept.* **364**, 175–246 (2002), [arXiv:hep-ph/0111114](#).
- [18] Piotr Salabura and Joachim Stroth, “Dilepton radiation from strongly interacting systems,” *Prog. Part. Nucl. Phys.* **120**, 103869 (2021), [arXiv:2005.14589 \[nucl-ex\]](#).
- [19] Frank Geurts and Ralf-Arno Tripolt, “Electromagnetic probes: Theory and experiment,” *Prog. Part. Nucl. Phys.* **128**, 104004 (2023), [arXiv:2210.01622 \[hep-ph\]](#).
- [20] Hendrik van Hees, Charles Gale, and Ralf Rapp, “Thermal Photons and Collective Flow at the Relativistic Heavy-Ion Collider,” *Phys. Rev. C* **84**, 054906 (2011), [arXiv:1108.2131 \[hep-ph\]](#).
- [21] Chun Shen, Ulrich W Heinz, Jean-Francois Paquet, and Charles Gale, “Thermal photons as a quark-gluon plasma thermometer reexamined,” *Phys. Rev. C* **89**, 044910 (2014), [arXiv:1308.2440 \[nucl-th\]](#).
- [22] See however the recent study of Ref. [69].
- [23] Ralf Rapp and Hendrik van Hees, “Thermal Dileptons as Fireball Thermometer and Chronometer,” *Phys. Lett. B* **753**, 586–590 (2016), [arXiv:1411.4612 \[hep-ph\]](#).
- [24] J. Adamczewski-Musch *et al.* (HADES), “Probing dense baryon-rich matter with virtual photons,” *Nature Phys.* **15**, 1040–1045 (2019).
- [25] As found in Refs. [70–72], the QGP source dominates over dileptons from a hadronic medium for $M > 1.1$ GeV.
- [26] Ulrich Heinz and Raimond Snellings, “Collective flow and viscosity in relativistic heavy-ion collisions,” *Ann. Rev. Nucl. Part. Sci.* **63**, 123–151 (2013), [arXiv:1301.2826 \[nucl-th\]](#).
- [27] Gabriel S. Denicol, Charles Gale, Sangyong Jeon, Akihiko Monnai, Björn Schenke, and Chun Shen, “Net baryon diffusion in fluid dynamic simulations of relativistic heavy-ion collisions,” *Phys. Rev. C* **98**, 034916 (2018),

- arXiv:1804.10557 [nucl-th].
- [28] Lipei Du and Ulrich Heinz, “(3+1)-dimensional dissipative relativistic fluid dynamics at non-zero net baryon density,” *Comput. Phys. Commun.* **251**, 107090 (2020), arXiv:1906.11181 [nucl-th].
- [29] Chun Shen and Sahr Alzhrani, “Collision-geometry-based 3D initial condition for relativistic heavy-ion collisions,” *Phys. Rev. C* **102**, 014909 (2020), arXiv:2003.05852 [nucl-th].
- [30] Akihiko Monnai, Björn Schenke, and Chun Shen, “Equation of state at finite densities for QCD matter in nuclear collisions,” *Phys. Rev. C* **100**, 024907 (2019), arXiv:1902.05095 [nucl-th].
- [31] H. A. Weldon, “Reformulation of finite temperature dilepton production,” *Phys. Rev. D* **42**, 2384–2387 (1990).
- [32] Charles Gale and Joseph I. Kapusta, “Vector dominance model at finite temperature,” *Nucl. Phys. B* **357**, 65–89 (1991).
- [33] J. I. Kapusta and Charles Gale, *Finite-temperature field theory: Principles and applications*, Cambridge Monographs on Mathematical Physics (Cambridge University Press, 2011).
- [34] Mikko Laine and Alekski Vuorinen, *Basics of Thermal Field Theory*, Vol. 925 (Springer, 2016) arXiv:1701.01554 [hep-ph].
- [35] Jessica Churchill, Lipei Du, Charles Gale, Greg Jackson, and Sangyong Jeon, “Dilepton production at NLO and intermediate invariant-mass observables,” (2023), arXiv:2311.06675 [nucl-th].
- [36] I. Ghisoiu and M. Laine, “Interpolation of hard and soft dilepton rates,” *JHEP* **10**, 083 (2014), arXiv:1407.7955 [hep-ph].
- [37] The overlap between the regimes cannot be neglected because α_s is not asymptotically small in practice.
- [38] Eric Braaten and Robert D. Pisarski, “Soft Amplitudes in Hot Gauge Theories: A General Analysis,” *Nucl. Phys. B* **337**, 569–634 (1990).
- [39] P. Aurenche, F. Gelis, G. D. Moore, and H. Zaraket, “Landau-Pomeranchuk-Migdal resummation for dilepton production,” *JHEP* **12**, 006 (2002), arXiv:hep-ph/0211036.
- [40] P. Aurenche, F. Gelis, and H. Zaraket, “Enhanced thermal production of hard dileptons by $3 \rightarrow 2$ processes,” *JHEP* **07**, 063 (2002), arXiv:hep-ph/0204145.
- [41] Peter Brockway Arnold, Guy D. Moore, and Laurence G. Yaffe, “Photon emission from ultrarelativistic plasmas,” *JHEP* **11**, 057 (2001), arXiv:hep-ph/0109064.
- [42] Peter Brockway Arnold, Guy D. Moore, and Laurence G. Yaffe, “Photon emission from quark gluon plasma: Complete leading order results,” *JHEP* **12**, 009 (2001), arXiv:hep-ph/0111107.
- [43] To be clear, we are only using the ‘leading-order’ LPM spectral function. Subsequent QCD corrections in this limit have been computed [73, 74].
- [44] R. Baier, B. Pire, and D. Schiff, “Dilepton production at finite temperature: Perturbative treatment at order α_s ,” *Phys. Rev. D* **38**, 2814 (1988).
- [45] Y. Gabellini, T. Grandou, and D. Poizat, “Electron - Positron Annihilation in Thermal QCD,” *Annals Phys.* **202**, 436–466 (1990).
- [46] T. Altherr and P. Aurenche, “Finite Temperature QCD Corrections to Lepton Pair Formation in a Quark - Gluon Plasma,” *Z. Phys. C* **45**, 99 (1989).
- [47] Joseph I. Kapusta, P. Lichard, and D. Seibert, “High-energy photons from quark - gluon plasma versus hot hadronic gas,” *Phys. Rev. D* **44**, 2774–2788 (1991), [Erratum: Phys.Rev.D 47, 4171 (1993)].
- [48] R. Baier, H. Nakkagawa, A. Niegawa, and K. Redlich, “Production rate of hard thermal photons and screening of quark mass singularity,” *Z. Phys. C* **53**, 433–438 (1992).
- [49] M. Laine, “Thermal 2-loop master spectral function at finite momentum,” *JHEP* **05**, 083 (2013), arXiv:1304.0202 [hep-ph].
- [50] M. Laine, “NLO thermal dilepton rate at non-zero momentum,” *JHEP* **11**, 120 (2013), arXiv:1310.0164 [hep-ph].
- [51] G. Jackson, “Two-loop thermal spectral functions with general kinematics,” *Phys. Rev. D* **100**, 116019 (2019), arXiv:1910.07552 [hep-ph].
- [52] G. Jackson and M. Laine, “Testing thermal photon and dilepton rates,” *JHEP* **11**, 144 (2019), arXiv:1910.09567 [hep-ph].
- [53] See Supplemental Material at [URL will be inserted by publisher] for a brief description of more technical details of this study.
- [54] DileptonEmission is a code designed to compute dilepton distributions with next-to-leading-order (NLO) emission rates at non-zero chemical potentials, integrated over a hydrodynamic spacetime evolution: <https://github.com/LipeiDu/DileptonEmission>.
- [55] iEBE-MUSIC is a comprehensive and fully-integrated numerical framework designed to streamline hybrid simulations for the study of relativistic heavy-ion collisions: <https://github.com/LipeiDu/iEBE-MUSIC>.
- [56] Lipei Du, Han Gao, Sangyong Jeon, and Charles Gale, “Rapidity scan with multistage hydrodynamic and statistical thermal models,” *Phys. Rev. C* **109**, 014907 (2024), arXiv:2302.13852 [nucl-th].
- [57] Doing so for the LPM contribution is challenging [75], and left for potential future work.
- [58] L. Adamczyk *et al.* (STAR), “Dielectron Mass Spectra from Au+Au Collisions at $\sqrt{s_{NN}} = 200$ GeV,” *Phys. Rev. Lett.* **113**, 022301 (2014), [Addendum: Phys.Rev.Lett. 113, 049903 (2014)], arXiv:1312.7397 [hep-ex].
- [59] L. Adamczyk *et al.* (STAR), “Measurements of Dielectron Production in Au+Au Collisions at $\sqrt{s_{NN}} = 200$ GeV from the STAR Experiment,” *Phys. Rev. C* **92**, 024912 (2015), arXiv:1504.01317 [hep-ex].
- [60] L. Adamczyk *et al.* (STAR), “Energy dependence of acceptance-corrected dielectron excess mass spectrum at mid-rapidity in Au+Au collisions at $\sqrt{s_{NN}} = 19.6$ and 200 GeV,” *Phys. Lett. B* **750**, 64–71 (2015), arXiv:1501.05341 [hep-ex].
- [61] M. I. Abdulhamid *et al.* (STAR), “Measurements of dielectron production in Au+Au collisions at $s_{NN}=27, 39$, and 62.4 GeV from the STAR experiment,” *Phys. Rev. C* **107**, L061901 (2023).
- [62] J. Cleymans, H. Oeschler, K. Redlich, and S. Wheaton, “Comparison of chemical freeze-out criteria in heavy-ion collisions,” *Phys. Rev. C* **73**, 034905 (2006), arXiv:hep-ph/0511094.
- [63] L. Adamczyk *et al.* (STAR), “Bulk Properties of the Medium Produced in Relativistic Heavy-Ion Collisions from the Beam Energy Scan Program,” *Phys. Rev. C* **96**, 044904 (2017), arXiv:1701.07065 [nucl-ex].
- [64] Those are labeled “cocktail” by the experimental collabo-

- ration. They are lepton pairs coming from the Drell-Yan process, from semi-leptonic decays of open flavor mesons, and from radiative decays of final-state hadrons.
- [65] R. Rapp, J. Wambach, and H. van Hees, “The Chiral Restoration Transition of QCD and Low Mass Dileptons,” *Landolt-Bornstein* **23**, 134 (2010), [arXiv:0901.3289 \[hep-ph\]](#).
- [66] Chun Shen and Björn Schenke, “Dynamical initial state model for relativistic heavy-ion collisions,” *Phys. Rev. C* **97**, 024907 (2018), [arXiv:1710.00881 \[nucl-th\]](#).
- [67] Giuliano Giacalone, Aleksas Mazeliauskas, and Sören Schlichting, “Hydrodynamic attractors, initial state energy and particle production in relativistic nuclear collisions,” *Phys. Rev. Lett.* **123**, 262301 (2019), [arXiv:1908.02866 \[hep-ph\]](#).
- [68] Lipei Du, Chun Shen, Sangyong Jeon, and Charles Gale, “Probing initial baryon stopping and equation of state with rapidity-dependent directed flow of identified particles,” *Phys. Rev. C* **108**, L041901 (2023), [arXiv:2211.16408 \[nucl-th\]](#).
- [69] Jean-François Paquet, “Thermal photon production in Gubser inviscid relativistic fluid dynamics,” (2023), [arXiv:2305.10669 \[nucl-th\]](#).
- [70] Ralf Rapp, “Dilepton Spectroscopy of QCD Matter at Collider Energies,” *Adv. High Energy Phys.* **2013**, 148253 (2013), [arXiv:1304.2309 \[hep-ph\]](#).
- [71] Gojko Vujanovic, Clint Young, Bjoern Schenke, Ralf Rapp, Sangyong Jeon, and Charles Gale, “Dilepton emission in high-energy heavy-ion collisions with viscous hydrodynamics,” *Phys. Rev. C* **89**, 034904 (2014), [arXiv:1312.0676 \[nucl-th\]](#).
- [72] Gojko Vujanovic, Jean-François Paquet, Gabriel S. Denicol, Matthew Luzum, Sangyong Jeon, and Charles Gale, “Electromagnetic radiation as a probe of the initial state and of viscous dynamics in relativistic nuclear collisions,” *Phys. Rev. C* **94**, 014904 (2016), [arXiv:1602.01455 \[nucl-th\]](#).
- [73] Jacopo Ghiglieri, Juhee Hong, Aleksi Kurkela, Egang Lu, Guy D. Moore, and Derek Teaney, “Next-to-leading order thermal photon production in a weakly coupled quark-gluon plasma,” *JHEP* **05**, 010 (2013), [arXiv:1302.5970 \[hep-ph\]](#).
- [74] Jacopo Ghiglieri and Guy D. Moore, “Low Mass Thermal Dilepton Production at NLO in a Weakly Coupled Quark-Gluon Plasma,” *JHEP* **12**, 029 (2014), [arXiv:1410.4203 \[hep-ph\]](#).
- [75] Sigtryggur Hauksson, Sangyong Jeon, and Charles Gale, “Photon emission from quark-gluon plasma out of equilibrium,” *Phys. Rev. C* **97**, 014901 (2018), [arXiv:1709.03598 \[nucl-th\]](#).
- [76] P. A. Baikov, K. G. Chetyrkin, and J. H. Kühn, “Five-Loop Running of the QCD coupling constant,” *Phys. Rev. Lett.* **118**, 082002 (2017), [arXiv:1606.08659 \[hep-ph\]](#).
- [77] S. Aoki *et al.* (Flavour Lattice Averaging Group), “FLAG Review 2019,” *Eur. Phys. J.* **C80**, 113 (2020), [arXiv:1902.08191 \[hep-lat\]](#).
- [78] Greg Jackson, “Shedding light on thermal photon and dilepton production,” *EPJ Web Conf.* **274**, 05014 (2022), [arXiv:2211.09575 \[hep-ph\]](#).
- [79] Dibyendu Bala, Sajid Ali, Anthony Francis, Greg Jackson, Olaf Kaczmarek, and Tristan Ueding, “Photon production rate from Transverse-Longitudinal (T–L) mesonic correlator on the lattice,” *PoS LATTICE2022*, 169 (2023), [arXiv:2212.11509 \[hep-lat\]](#).
- [80] Lipei Du, “Bulk medium properties of heavy-ion collisions at beam energy scan with a multistage hydrodynamic model,” (2023), [arXiv:2401.00596 \[hep-ph\]](#).

SUPPLEMENTAL MATERIAL

Running coupling

For phenomenology, the value of the QCD gauge coupling in our approach needs to be specified. The coupling is a function of the energy scale Q and obeys the renormalization group equation $\partial_t a_s = -\sum_{k=1}^{\ell} \beta_{k-1} a_s^{k+1}$ to ℓ -loop accuracy, where $a_s \equiv \alpha_s(Q)/\pi$ and $t \equiv \log(Q^2/\Lambda_{\overline{\text{MS}}}^2)$. The coefficients $\beta_0, \beta_1, \beta_2, \beta_3, \beta_4$ can be found in Ref. [76]. Figure S1 (left) shows the resulting dependence on Q in GeV, for $\ell \leq 5$. (For $n_f = 3$ we use $\Lambda_{\overline{\text{MS}}} = 343$ MeV to set physical units [77].) In the calculation of the dilepton rate, we should evaluate $\alpha_s(Q)$ at the ‘optimal’ scale which should depend on those among M, T, μ_B . Rigorously, the choice of Q should emerge from higher order QCD corrections than we are considering. Since we make use of the spectral function in the IMR, we have to be pragmatic and adopt a procedure which is compatible with the limits in which Q is known. For example, one could take the geometric mean (a slightly different choice was made in Ref. [36]):

$$Q_{\text{opt}} = \sqrt{M^2 + (2\pi T)^2 + \frac{1}{9} \mu_B^2}. \quad (\text{A.1})$$

This choice is motivated by the fact that when one of the three scales M, T or μ_B is much larger than the other two, then Q_{opt} should be set by that dominant parameter. At $\mu_B = 0$, this choice was also found to give relatively good agreement with non-perturbative lattice data for the Euclidean correlator [52, 78, 79].

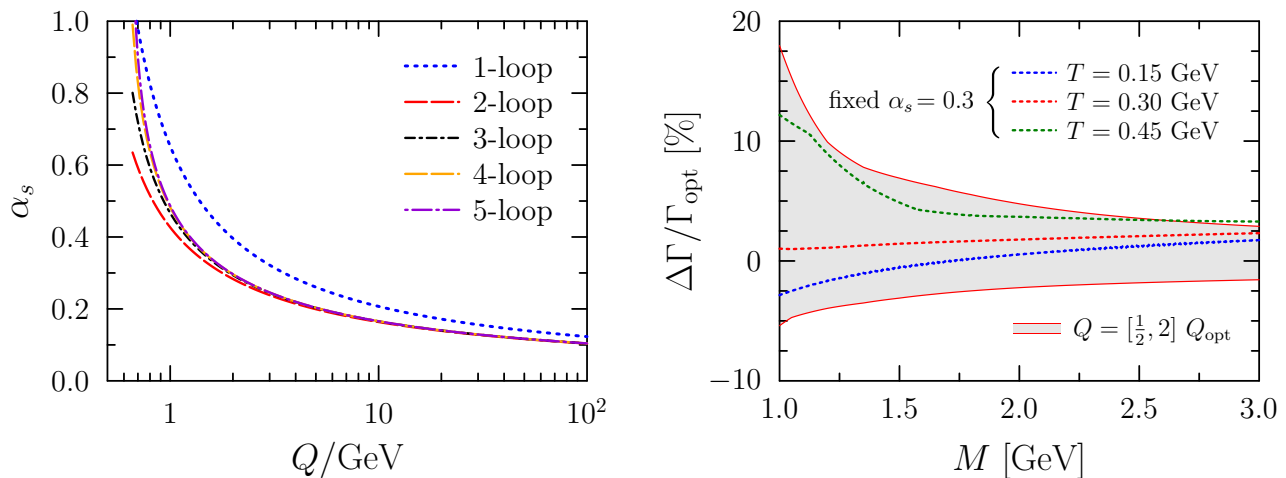


Figure S1. Left: Value of the QCD coupling as a function of the renormalisation scale Q , at various loop levels. Right: Illustration of the percentual effect from the running coupling, in the IMR. Here we show a ratio, taken w.r.t. to the observable $d\Gamma/dM$ for a point source (cf. Fig. 6 in Ref. [35]). The denominator is defined by using the 5-loop running coupling, evaluated at $Q = Q_{\text{opt}}$ from (A.1), and the gray band shows the deviation from varying this choice by a factor of 2 (for $T = 0.30$ GeV). Using a fixed coupling $\alpha_s = 0.3$ gives the dotted lines, shown for $T = 0.15, 0.30, 0.45$ GeV. (In this figure, $\mu_B = 0$.)

In order to assess the uncertainty in our perturbative predictions, we vary the renormalization scale in the range $Q \in [\frac{1}{2}, 2] \times Q_{\text{opt}}$. To avoid intrinsic difficulties of QCD in the far infrared, which reflects in (A.1) when M, T and μ_B are simultaneously small, we do not allow the coupling to exceed unity: $\alpha_s \leq 1$. (The corresponding dilepton rates in this regime are in any case small, and do not contribute significantly to the total yield.) For simplicity, we consider the \mathbf{k} -integrated rate from a static point source as done in Ref. [35]. In this setting, we obtain the right hand side plot in Fig. S1 which depicts the relative importance of the running coupling as a function of M . We can make two observations: Firstly, the sensitivity to varying the scale (at $T = 0.3$ GeV) diminishes from 10% for $M \lesssim 1$ GeV to 2% for $M \gtrsim 3$ GeV. Secondly, using a fixed value of $\alpha_s = 0.3$ appears to be accurate to a few percent for $M \gtrsim 1.5$ GeV.

Temperature extraction in time

In this section, we elaborate on the methodology for conducting a comparative analysis between T_{eff} derived from dilepton spectra and the evolving hydrodynamic temperatures at individual time steps. For T_{eff} , we compute dilepton production from all fluid cells at each time step and extract the corresponding T_{eff} values from the spectra. To quantify the spatially fluctuating hydrodynamic temperatures, which arise from the system's intrinsic inhomogeneity, we compute both the mean ($\langle T \rangle$) and standard deviation ($\langle \delta T \rangle$) for fluid cells at each time step. In these calculations, the temperature of each fluid cell (within spacetime rapidity window $|\eta_s| < 1$) is weighted by its energy density (e) multiplied by the Lorentz boost factor ($\gamma = u^t$), following what is done in the MUSIC package. The weighting factor considers that fluid cells with varying temperatures do not contribute equally to the observables. Instead, their contribution is proportional to their energy (or entropy) density.

Figure S2 depicts the comparison between effective temperature and hydrodynamic temperature as functions of the proper time for Au+Au collisions at two selected beam energies within centrality classes ranging from 0–10% to 70–80%. The dots interconnected by lines represent the effective temperatures T_{eff} derived from the dilepton spectra, while the curves accompanied by bands represent the mean value ($\langle T \rangle$) and standard deviation ($\langle \delta T \rangle$) of hydrodynamic temperatures. The figure demonstrates a close alignment between T_{eff} and the hydrodynamic temperatures. The initial mean value ($\langle T_{\text{in}} \rangle$) and standard deviation ($\langle \delta T \rangle$) of temperatures, along with the corresponding proper time (τ_0), when the hydrodynamic evolution starts for the eight beam energies across eight centrality classes, are listed in Table S1. In this work, the values of τ_0 are obtained from Ref. [29], initially motivated by the overlap time between the two colliding nuclei and further adjusted to reproduce the mean transverse momentum of identified particles [29, 80].

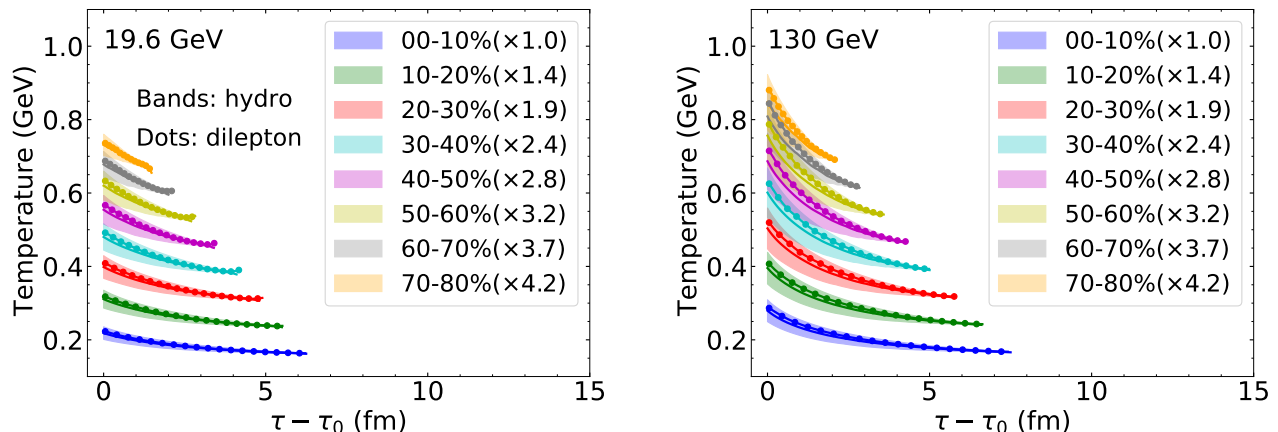


Figure S2. Comparison of effective temperatures derived from dilepton spectra (dots) and the hydrodynamic temperatures (bands) across various proper times, for Au+Au collisions within a range of centrality classes from 0–10% to 70–80% at two selected beam energies. To enhance clarity in the visualization, distinct multiplicative factors are applied to the temperatures corresponding to various centrality classes. The solid curve for hydrodynamic temperatures represents the mean values, with the band width indicating the standard deviations; see the texts for details.

Table S1. Initial mean temperature ($\langle T_{\text{in}} \rangle$) and standard deviation ($\langle \delta T \rangle$), as well as effective temperature (T_{eff}), along with the initial proper time (τ_0), for different beam energies and centrality classes.

$\sqrt{s_{\text{NN}}}$ (GeV)	τ_0 (fm)	T (MeV)	Centrality							
			0–10%	10–20%	20–30%	30–40%	40–50%	50–60%	60–70%	70–80%
7.7	3.6	T_{in}	178 ± 12	175 ± 12	172 ± 12	169 ± 12	164 ± 11	159 ± 11	153 ± 11	144 ± 11
		T_{eff}	173 ± 0	171 ± 0	170 ± 0	167 ± 0	165 ± 0	161 ± 0	157 ± 0	150 ± 0
19.6	1.8	T_{in}	218 ± 17	214 ± 17	210 ± 16	204 ± 15	198 ± 14	191 ± 12	183 ± 10	176 ± 7
		T_{eff}	199 ± 1	197 ± 1	194 ± 1	191 ± 1	187 ± 1	183 ± 0	177 ± 0	173 ± 0
27	1.4	T_{in}	235 ± 21	231 ± 20	225 ± 20	219 ± 19	211 ± 18	202 ± 16	193 ± 13	184 ± 10
		T_{eff}	209 ± 2	207 ± 2	204 ± 2	201 ± 2	196 ± 1	191 ± 1	184 ± 1	179 ± 0
39	1.0	T_{in}	260 ± 26	254 ± 26	247 ± 25	239 ± 25	230 ± 23	219 ± 21	208 ± 18	196 ± 15
		T_{eff}	223 ± 4	221 ± 3	218 ± 3	214 ± 3	209 ± 2	202 ± 2	195 ± 1	187 ± 1
54.4	1.0	T_{in}	265 ± 27	259 ± 27	252 ± 26	244 ± 26	234 ± 24	223 ± 22	211 ± 19	198 ± 16
		T_{eff}	227 ± 4	224 ± 4	221 ± 3	217 ± 3	211 ± 2	205 ± 2	197 ± 1	189 ± 1
62.4	1.0	T_{in}	268 ± 27	262 ± 27	255 ± 27	246 ± 26	236 ± 25	225 ± 23	212 ± 19	200 ± 16
		T_{eff}	229 ± 4	226 ± 4	223 ± 3	219 ± 3	213 ± 3	206 ± 2	198 ± 2	190 ± 1
130	1.0	T_{in}	279 ± 30	273 ± 30	265 ± 29	256 ± 29	245 ± 27	233 ± 25	219 ± 21	204 ± 18
		T_{eff}	236 ± 5	234 ± 4	230 ± 4	225 ± 4	219 ± 3	212 ± 2	203 ± 2	194 ± 1
200	1.0	T_{in}	290 ± 32	283 ± 32	275 ± 31	265 ± 31	253 ± 29	240 ± 27	225 ± 24	210 ± 20
		T_{eff}	244 ± 5	242 ± 5	238 ± 5	233 ± 4	226 ± 4	218 ± 3	209 ± 2	198 ± 1